A novel nitridation- and pesting-resistant Cr-Si-Mo alloy

Frauke Hinrichs [a], Alexander Kauffmann [a] *, Aditya Srinivasan Tirunilai [a], Daniel Schliephake [a], Bonita Beichert [a], Georg Winkens [a], Katharina Beck [c], Anke Silvia Ulrich [c], Mathias Christian Galetz [c], Zhongmin Long [b], Hemanth Thota [b], Yolita Eggeler [b], Astrid Pundt[a] and Martin Heilmaier[a]

[a] Institute for Applied Materials (IAM), Karlsruhe Institute of Technology (KIT), Engelbert-Arnold-Str. 4, 76131 Karlsruhe, Germany

[b] Microscopy of Nanoscale Structures & Mechanisms, Laboratory for Electron Microscopy (LEM), Karlsruhe Institute of Technology (KIT), Wolfgang-Gaede Str.1a, 76131 Karlsruhe, Germany

[c] DECHEMA-Forschungsinstitut, High Temperature Materials, Theodor-Heuss-Allee 25, 60486 Frankfurt am Main, Germany

* corresponding author
mail: alexander.kauffmann@kit.edu (A. Kauffmann)
phone: +49 721 608 42346

Highlights

- Pesting resistance is obtained at 800 °C for Cr-13.5Si-32.2Mo (at.%)
- Monolithic σ phase in Cr-Si-Mo system decomposes into A2 solid solution and A15 intermetallic
- Outstanding oxidation at 800 °C and reasonable oxidation resistance up to 1200 °C is obtained for 100 h
- Protective Cr_2O_3 scales form, no nitridation or spallation occurs at 800 - 1200 °C up to 100 h

Abstract

Cr-13.5Si-32.2Mo (at.%) solidifies as metastable σ-phase with a dendritic microstructure during arc melting. Heat treatment leads to a decomposition into a fine-lamellar microstructure of $(Cr,Mo)_{ss}$ and $(Cr,Mo)_3Si$. A protective Cr_2O_3 layer with low growth rates was formed upon cyclic oxidation at 800, 1100 and 1200 °C for up to 100 h. In addition to the Cr_2O_3 layer, the formation of an internal silicon oxide layer is found for 1200 °C. Oxidation scales show parabolic growth rates at 1100 and 1200 °C. Up to 100 h, the oxidation occurred remarkably free of nitridation, spallation or pesting.

Keywords

Cr-Si-Mo, Cyclic Oxidation, Pesting Resistance, Silicides, σ Phase

1 Introduction

To further improve the efficiency of turbines, it is inevitable to develop new high temperature structural materials, which can exceed the operation temperatures of currently used Ni-based alloys. Hence,

refractory metals and alloys have come into focus of research due to their high melting points. However, refractory metal alloys usually suffer from poor oxidation resistance at elevated temperatures [1] [1]. Significant progress with respect to the oxidation resistance was made in the development of oxidation-resistant Mo-Si-Ti alloys [2–4]. Unlike other Mo-Si-based alloys with volume fractions of the solid solution around or beyond 50 %, some eutectic and eutectic-eutectoid Mo-Si-Ti alloys were found to withstand catastrophic failure in the so-called pesting regime around 800 °C, when the formation of volatile MoO_3 becomes dominant and therefore detrimental to the material. Those pesting-resistant Mo-Si-Ti alloys form protective scales consisting of a mixture of TiO_2 and SiO_2 [2,4], despite the expected non-protective nature of TiO_2 at high temperatures [5–7].

In Ref. [3] it was shown, that pesting resistance in Mo-Si-Ti alloys is mainly determined by the Ti content. A minimum Ti content of 34 at.% in the solid solution and 43 at.% in the nominal alloy composition is required. However, even in pesting resistant Mo-Si-Ti alloys, phase specific oxidation of the Ti containing Mo solid solution is observed. At the transition between pesting and pesting-resistant compositions, the microstructural dimensions also influence pesting resistance. These fine-lamellar, two-phase microstructures consist of a body centered cubic (bcc) solid solution (Strukturbericht A2, W prototype, space group no. 229) and hexagonal or tetragonal silicides ($D8_8$, Mn_5Si_3, no. 193 or $D8_m$, W_5Si_3, no. 140), respectively. Hence, they may profit from the high temperature strength and oxidation resistance of the intermetallic phases, while the high amount of bcc solid solution promises processing capability. Therefore, future alloy design should focus also on other fine-lamellar microstructures consisting of a solid solution and an intermetallic compound. New alloy strategies need to address the question, how similar microstructural features compare to the Mo-Si-Ti alloys with respect to the oxidation resistance in the pesting regime and if selective oxidation of the solid solution phase can be minimized or avoided through a homogeneous distribution of the passivating elements between the solid solution and intermetallic phases.

As the large amount of Ti leads to an unexpectedly protective oxide scale, similar or even superior results might be achieved through alloying with elements, which are considered passivating such as Cr. Alloying with Cr (instead of Ti) to produce a protective Cr_2O_3 scale is promising for several reasons: (i) There is a complete solubility in the binary Mo-Cr system similar to the Mo-Ti at high temperatures [8]. (ii) With 1907 °C, the melting point of Cr is higher than that of Ti and the solid solution strengthening in binary $(Cr,Mo)_{ss}$ (A2, W, no. 229) is stronger than in Mo-Ti [9]. These two aspects indicate even better high temperature mechanical properties than of the eutectic Mo-Si-Ti alloy [2]. Regarding the intermetallic phase, desired by the alloy strategy, $(Cr,Mo)_3Si$ (A15, Cr_3Si, no. 223) is obtained [10] with a complete solubility between Mo_3Si and Cr_3Si. The $(Cr,Mo)_{ss}$ and $(Cr,Mo)_3Si$ notations are used throughout the manuscript to emphasize that Mo is in solution in both phases, substituting Cr sites. Due to the complete solubility of both constituting phases, a ternary, two-phase alloy consisting of $(Cr,Mo)_{ss}$ and $(Cr,Mo)_3Si$ might, thus, enable the homogenous formation of a Cr_2O_3 scale and protect the Mo-rich solid solution from pesting.

Although the oxidation behavior of pure Cr, Cr-Si alloys as well as Mo-Si alloys, have been studied in literature already, there is not much data on the oxidation behavior of Cr-Mo solid solutions, nor Cr-Mo-Si for Si contents of < 24 at.% with high amounts of Mo-rich solid solution. For an overview on the challenges in developing high temperature alloys in both alloy systems, the reader may be referred to Refs. [1,11,12]. For pure Cr, it is known at elevated temperatures not only Cr_2O_3 is formed, but volatile CrO_3 as well [13]. At temperatures above 1000 °C, the rate of CrO_3 evaporation becomes faster than the rate of Cr diffusion through the oxide to react with oxygen so that the oxide layer loses its protectiveness [13]. Apart from this, a large volume misfit between Cr and its oxide and differences in thermal

expansion, were claimed responsible for the deterioration of the adhesion between oxide and substrate, leading to massive spallation [14]. Additionally, the inward diffusion of N led to the formation of a nitride layer below the outer Cr_2O_3 scale [15]. Alloying Cr with Si and/or Mo improves the oxidation and nitridation resistance [16]. The majority of oxidation experiments with relevance to the Cr-Si-Mo system have however been carried out with compositions either in or close to the binary Cr-Si system [11,17,18] or with high Si contents in the ternary system [19–21], thus avoiding the occurrence of large amounts of a Mo-containing solid solution.

Rudy and Nowotny [22] revealed that in the ternary Cr-Si-Mo system a σ phase ($D8_b$, Cr_6Fe_7, no. 136) forms under non-equilibrium, fast cooling conditions in the composition range from 57Cr-29Mo-14Si to 39Cr-47Mo-14Si (unless stated otherwise at.% are used throughout the article). Heat treatments above 1150 °C lead to a decomposition of the σ phase solid state reaction, forming a fine-lamellar microstructure of $(Cr,Mo)_{ss}$ and $(Cr,Mo)_3Si$ [22].

Hence, with respect to the Cr-Si-Mo system, the aforementioned research questions are refined to

i. How do fine-lamellar Mo-Si-Cr alloys compare to similar Mo-Si-Ti or Cr-based alloys with respect to oxidation resistance, especially in the pesting regime at about 800 °C with potential MoO_3 evaporation [23,24] and beyond 1000 °C where CrO_3 starts to evaporate [11,25]?
ii. How does solute partitioning of Cr in Mo-Si-Cr compare to Ti in Mo-Si-Ti in view of the continuous phase fields of $(Cr,Mo)_{ss}$ and $(Cr,Mo)_3Si$ and does a homogeneous distribution of Cr lead to a uniform oxidation of both phases?

2 Experimental and materials

2.1 Material synthesis

The Cr-13.5Si-32.2Mo alloy was identified as composed of σ phase only in preliminary work and, therefore, synthesized from pure Mo foils (EVOCHEM, 99.95 %) Si pieces (ChemPur, 99.99 %) and Cr granules (ChemPur 99.99%) by arc melting. Arc melting was performed using an AM/0,5 Arc Melter (Edmund Bühler GmbH), equipped with a water-cooled Cu crucible for ingot casting. The chamber was evacuated and flooded with Ar of > 99.998 % purity at least three times. In the last evacuation cycle, the chamber was pumped down to less than $1 \cdot 10^{-4}$ mbar. Subsequently the chamber was vented with Ar to a base pressure of 600 mbar for arc melting. The ingots were flipped and remelted five times to ensure homogeneity. To evaluate the as-cast microstructure, samples were taken for microstructural analyses. Prior to all oxidation experiments, the ingots were heat treated for 100 h at 1200 °C in a protective Ar atmosphere (> 99,998 % purity). For heat treatments, a HTRH 70-600/18 resistance tube furnace (Carbolite GeroGmbH & Co. KG) was used. To protect the ingots from impurities in the Ar atmosphere Ti sponge was used as getter material in the tube furnace. No O uptake was detected.

2.2 Microstructure analysis

Samples for microstructural analysis in the as-cast (AC), heat-treated (HT) and oxidized condition were cold mounted in VariKem 200 resin, ground to grit P2500 with SiC grinding paper followed by 3 and 1 µm diamond polishing steps. Surface finish was achieved using a colloidal OP-S suspension (Buehler ITW). Backscattered electron contrast imaging (BSE) micrographs of AC and HT as well as the oxide scales were taken at 20 kV on a LEO Gemini 1530 (Carl Zeiss AG) scanning electron microscope (SEM). Volume fractions of solid solution and silicide phase in the HT condition were determined from BSE micrographs using the open source image processing software ImageJ (version 1.53c) [26]. SEM-based energy-dispersive X-ray spectroscopy (SEM-EDS) was performed on an Auriga 60 (Carl Zeiss

AG) SEM equipped with an Octane Super EDS detector. For EDS analysis the SEM was operated at 14 kV acceleration voltage.

The phases present in the bulk material, as well as the phases formed during cyclic oxidation were investigated through X-ray diffraction (XRD) using a D2 Phaser (Bruker). The XRD device is equipped with a LynxEye line detector and the Cu tube was operated at 30 kV and 10 mA. The scans were performed at a step size of 0.01° in 2Θ. The cubic lattice parameters of the $(Cr,Mo)_{ss}$ and the $(Cr,Mo)_3Si$ were determined by extrapolating towards $\Theta = 90°$, using the weight function $\frac{1}{2}(\cot^2\Theta + \cot\Theta\cos\Theta)$ similar to Nelson and Riley (NR) [27]. In addition, the chemical composition/Cr/Mo ratio was determined by back calculations. For microstructure and NR analysis of the AC and HT condition, XRD was performed on bulk cross sections, which were ground to grit P2500. Oxide scale XRD analysis was performed on the as-oxidized sample surface without any further metallographic preparation.

Energy dispersive X-ray spectroscopy (EDS) using a transmission electron microscope (TEM) was used to determine the local chemical composition of the individual phases in the non-oxidized HT condition and to analyze the oxide scale after cyclic oxidation at 800 °C for 100 h. A TEM lamella was prepared using a FEI Strata 400S Focused Ion Beam with a Ga Ion source. EDS was performed on a FEI Osiris TEM in high-angle annular dark-field scanning transmission electron microscopy (HAADF-STEM) mode with an acceleration voltage of 200 kV. The EDS spectra are quantified in an automatic manner using standard procedure implemented in the Bruker Esprit 2.3 software employing thin film approximation of the TEM lamella with theoretical Cliff-Lorimer parameters.

2.3 Cyclic oxidation

Prior to oxidation in air, cuboidal samples of $(5 \times 5 \times 5)$ mm^3 in dimensions were cut from HT material by electrical discharge machining. All sides of the cuboids were ground to grit P2500 after machining in order to avoid any influence by the prior treatment of the material. Before oxidation, the sample surface area was obtained through area measurements using the software Olympus Stream Enterprise 1.7 (Olympus) and a Wild-Heerbrugg M420 optical macroscope. For cyclic oxidation HT material was used exclusively. Cyclic oxidation was performed at 800 (pesting regime), 1100 (potential limit of operation of the present alloy), and 1200 °C (significant evaporation of chromia is expected) in laboratory air using muffle furnaces (Gero and Nabertherm). The duration and sequence of oxidation cycles was performed according to the scheme described in Ref. [28]. Mass changes of the oxidation samples were tracked after each oxidation cycle using a Sartorius precision balance with an accuracy of 1 µg up to a total duration of 100 h. Oxide scale thicknesses were determined by processing BSE micrographs of sample cross sections using ImageJ

3 Results

3.1 Microstructure and chemical composition

The overall chemical composition of the arc-melted ingot was analyzed through EDS analysis to be (55.0 ± 0.2)Cr-(13.3 ± 0.1)Si-(31.7 ± 0.3)Mo. The deviation from the nominal composition is considered to lie well within the limits of EDS measurements. Figs. 1a and b show BSE micrographs of the alloy in the AC and HT condition with an overview in the upper part of the image and magnifications below. The corresponding XRD patterns are shown in Figs. 1c and d. In the AC condition, a dendritic microstructure for Cr-13.5Si-32.2Mo is obtained as seen in Fig. 1a. The dendritic and interdendritic regions exhibit continuous transitions in BSE (atomic number Z) contrast. Results from SEM-EDS point analysis of the bright and dark regions in the BSE micrographs are presented in Tab. 1. At least three

measurements were taken and averaged in each region. The Si content varies by only 3 at.% between the two regions, whereas the Cr and Mo content vary by roughly 10 at.%. XRD analysis reveals a monolithic tetragonal σ phase, represented by green triangles in Fig. 1c, in agreement with Rudy and Nowotny [22] for a similar composition range in the Mo-Si-Cr system. The difference in Cr and Mo content between the apparently brighter and darker regions (in BSE) do not significantly affect the lattice parameters.

Figs. 1b and d prove the solid state decomposition of the σ phase during a heat treatment in protective Ar atmosphere at 1200 °C for 100 h. In the HT condition, no σ phase is detected anymore. The HT material consists of $(Cr,Mo)_{ss}$ and $(Cr,Mo)_3Si$ with (44 ± 2) and (56 ± 2) vol.%, respectively, as determined by binarization and pixel analysis of BSE micrographs. The STEM HAADF inlet in Fig. 1b represents a cross section through the lamellar microstructure. The pattern in the light grey $(Cr,Mo)_{ss}$ lamellae is an artefact from FIB sample preparation. With the NR analysis of the XRD pattern, the cubic lattice parameters *a* for $(Cr,Mo)_{ss}$ and $(Cr,Mo)_3Si$ were determined. Fig. 2 depicts the literature lattice parameters of binary $(Cr,Mo)_{ss}$ (Fig. 2a) and quasi-binary $(Cr,Mo)_3Si$ intermetallic solutions (Fig. 2b) as a function of the dissolved Cr content in the respective phase as black lines. The lattice parameter of pure Mo marks the left axis of Fig 1a. By alloying Cr to Mo, Mo sites in the solid solution are substituted by Cr atoms, hence decreasing the lattice parameter. A similar trend applies to the quasi-binary intermetallic solution in Fig. 2b with the left and right axis marking the lattice parameter of Mo_3Si and Cr_3Si, respectively. The progression of *a* was used to estimate the chemical composition of each phase in HT Cr-13.5Si-32.2Mo. The points in Figs. 2a and b indicate the determined lattice parameters of the two phases present in Cr-13.5Si-32.2Mo, e.g. 3.006 Å for $(Cr,Mo)_{ss}$ and 4.696 Å for $(Cr,Mo)_3Si$. These are in good agreement with Ref. [22], reporting *a* to lie between 2.98–3.02 Å for $(Cr,Mo)_{ss}$ and 4.69–4.71 Å for $(Cr,Mo)_3Si$ for phases within a similar composition range. The corresponding ranges of Cr contents of constituting phases in the present alloy are marked by blue and red shaded regions on the composition axis. These were recalculated considering a conservative error of lattice parameter determination of ± 0.005 Å, not further resolving the inhomogeneous Cr concentrations by the dendritic microstructure that are *not* homogenized during the heat treatment (see Fig. 1a). The change in lattice parameter by Si is small and therefore neglected in the present analysis [29,30]. The arrows show the nominal Cr content in the alloy for comparison. Furthermore, the results for the alloy's chemical composition obtained through SEM-EDS, TEM-EDS and NR analysis of $(Cr,Mo)_{ss}$ and $(Cr,Mo)_3Si$ phase are listed in Tab. 1.

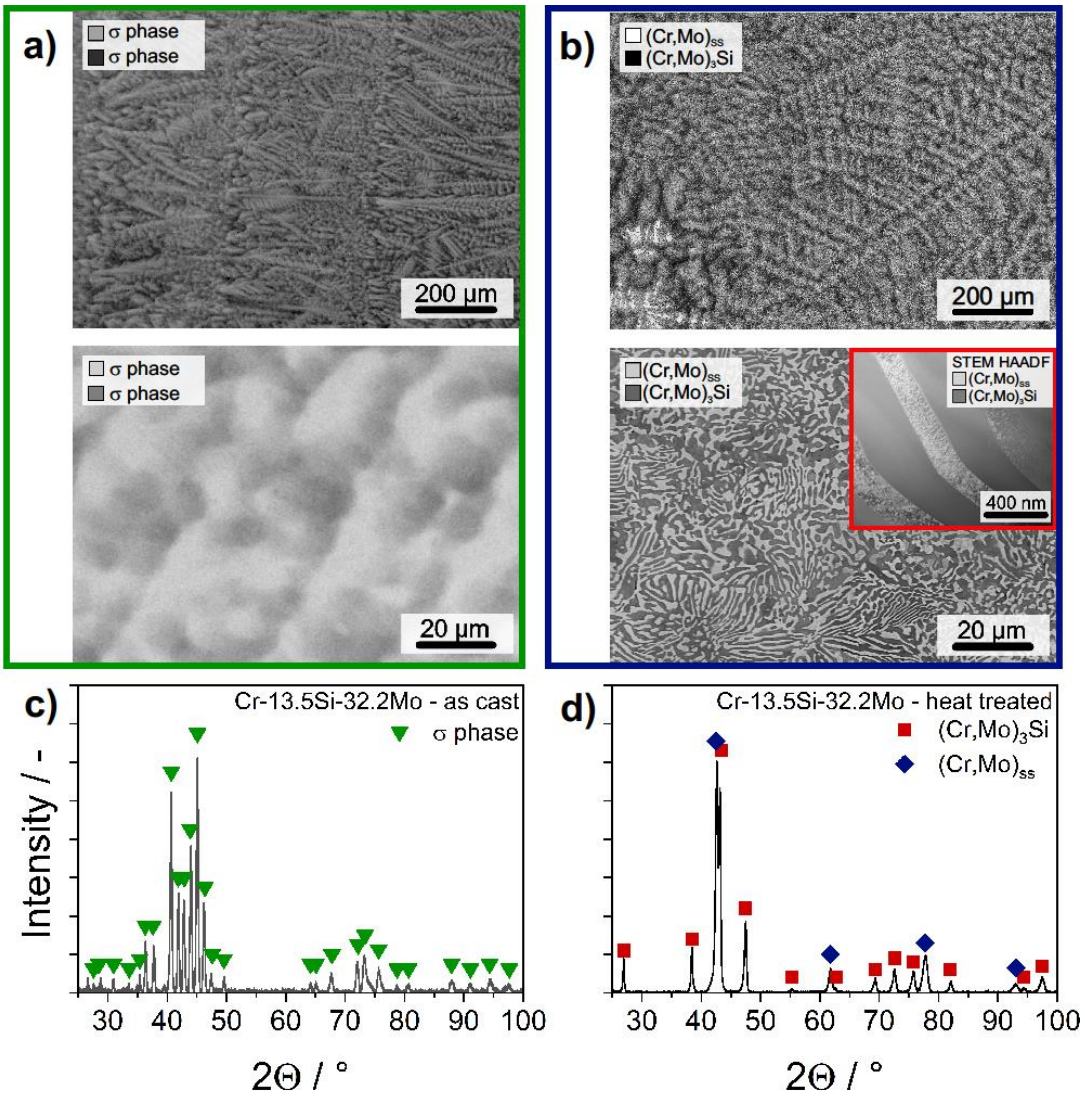

Fig. 1: BSE micrographs, overview and magnifications of a) the AC microstructure (almost monolithic σ phase with dendritic microstructure) and b) HT microstructure (fine-lamellar, two-phase microstructure). The inset in b) shows a STEM HAADF image of the lamellar regions. c) and d) show corresponding XRD patterns with peak positions of the identified phases.

Tab. 1: Chemical composition of the alloy and compositions of the constituting phases in the AC and HT condition according to SEM-EDS, STEM-EDS and back calculation from XRD. Errors noted for SEM- and STEM-EDS represent the standard deviations of at least three individual measurements.

	Phase/Region	Method	Mo / at.%	Si / at.%	Cr / at.%	Mo/Cr ratio
Desired composition	Total	–	32.2	13.5	54.3	0.59
Experimental composition		SEM-EDS	31.7 ± 0.3	13.3 ± 0.1	55.0 ± 0.2	0.58
AC	σ, light grey	SEM-EDS	37.0 ± 0.7	12.1 ± 0.1	50.9 ± 0.6	0.73
	σ, dark grey		24.4 ± 1.0	15.3 ± 0.2	60.3 ± 0.8	0.40
HT	$(Cr, Mo)_{ss}$	SEM-EDS	42.8 ± 0.9	2.1 ± 0.1	55.1 ± 0.8	0.78
		STEM-EDS	44.8 ± 0.9	5.2 ± 1.0	50.0 ± 1.8	0.90
		XRD		–		0.74
	$(Cr,Mo)_3Si$	SEM-EDS	25.1 ± 0.1	19.0 ± 0.0	55.6 ± 0.1	0.45
		STEM-EDS	29.3 ± 0.1	26.2 ± 0.3	44.5 ± 0.4	0.66
		XRD		–		0.55

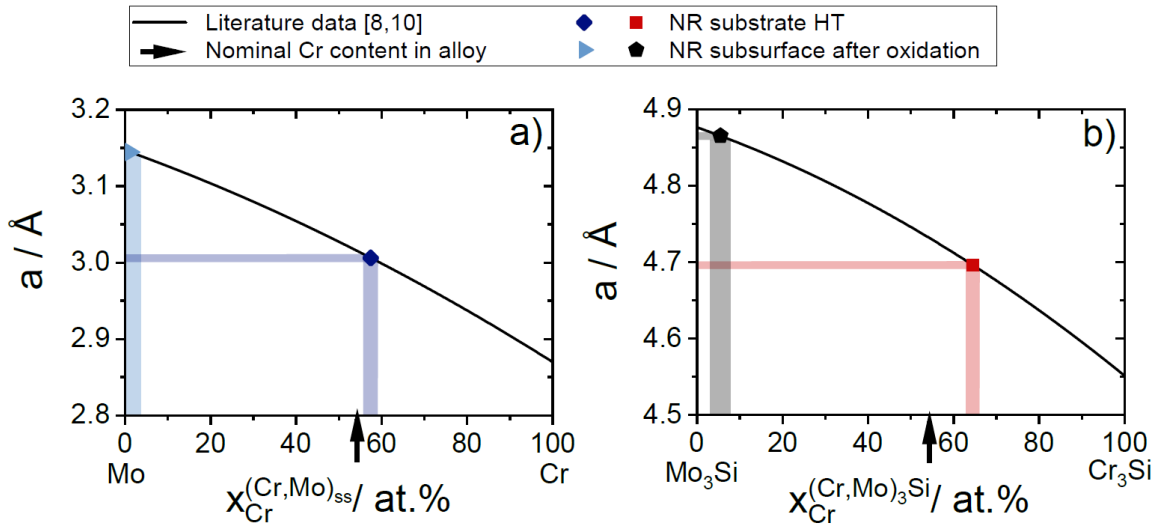

Fig. 2: Lattice parameters *a* in the binary $(Cr,Mo)_{ss}$ and $(Cr,Mo)_3Si$ solutions. Black lines represent literature data from Refs. [8,10]. Lattice parameters *a* of the respective phases in Cr-13.5Si-32.2Mo, determined from XRD patterns by NR analysis are projected to the literature reference with an error of ± 0.005 Å as highlighted by horizontal bars. This corresponds to a range of Cr content, indicated by the vertical columns. The arrows indicate the nominal overall Cr content in the alloy. The light blue and black symbols on the Mo-rich sides, belong to surface-near solid solution and silicide seen in oxidized samples that are significantly depleted in Cr due to the oxidation process.

3.2 Cyclic oxidation

Fig. 3a displays a selection of oxidation samples after oxidation for 100 h for the temperatures tested. Figs. 3b-d show the specific mass change as a function of time during cyclic oxidation at 800 (pesting regime), 1100 (potential limit of operation of the present alloy), and 1200 °C (significant evaporation of chromia is expected) for three samples tested at each temperature. Figs. 4a-d shows BSE images of cross sections of oxidized specimen after various oxidation times. STEM-EDS and SEM-EDS mappings of the oxidation scales forming at 800, 1100 and 1200 °C are shown in Figs. 4e, f and g. The diffraction patterns obtained for the oxidized Cr-Si-Mo samples after 100 h of cyclic oxidation are given in Fig. 5. As indicated by the orange circles in Fig. 5, α-Cr_2O_3 chromia (corundum prototype, no. 167) was identified to form as a top layer at all temperatures.

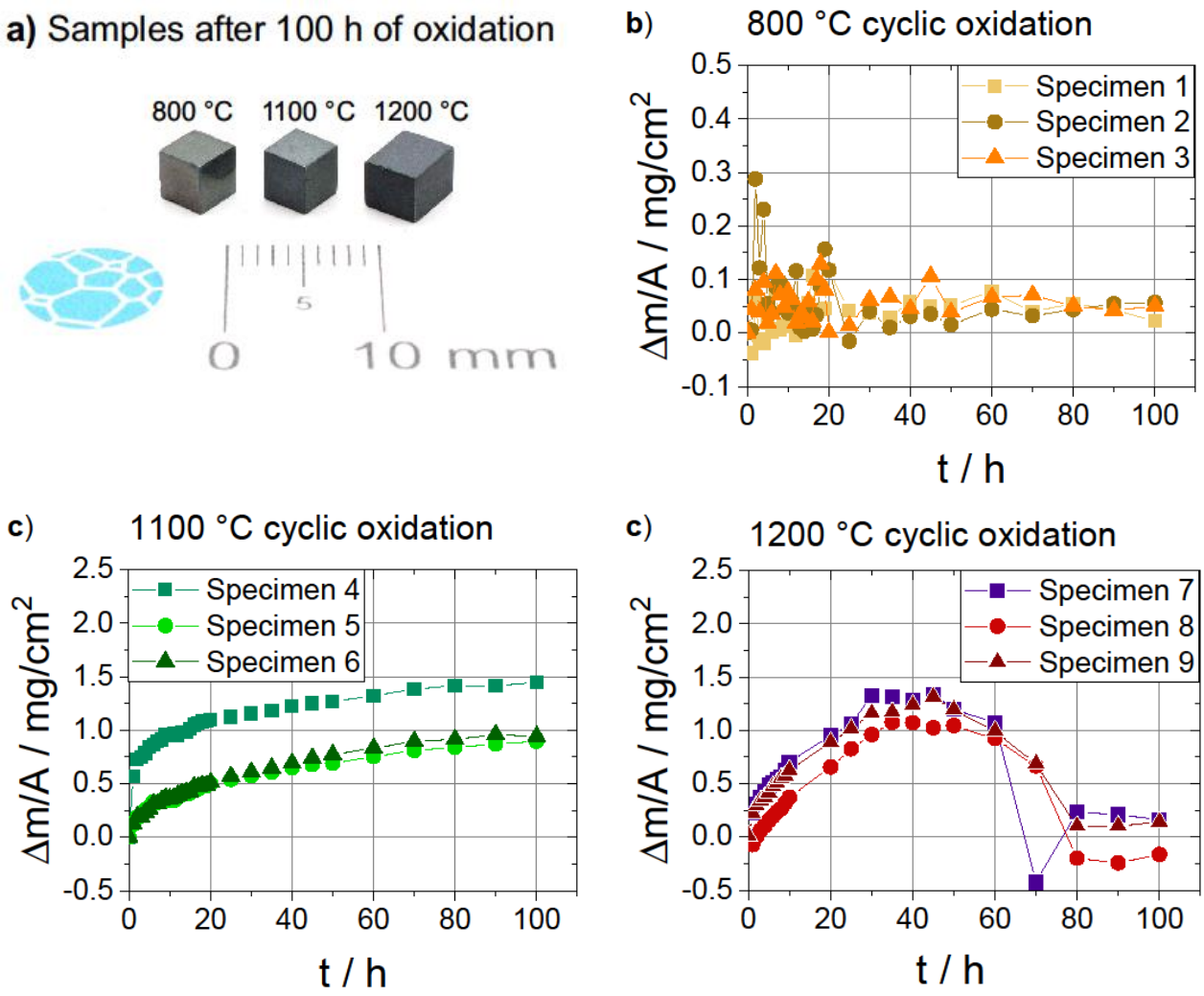

Fig. 3: a) Macroscopic sample images after 100 h at 800, 1100, 1200 °C and specific mass change for cyclic oxidation in laboratory air up to 100 h at b) 800, c) 1100 and d) 1200 °C. Note the different scaling of the diagram for 800 °C in c.

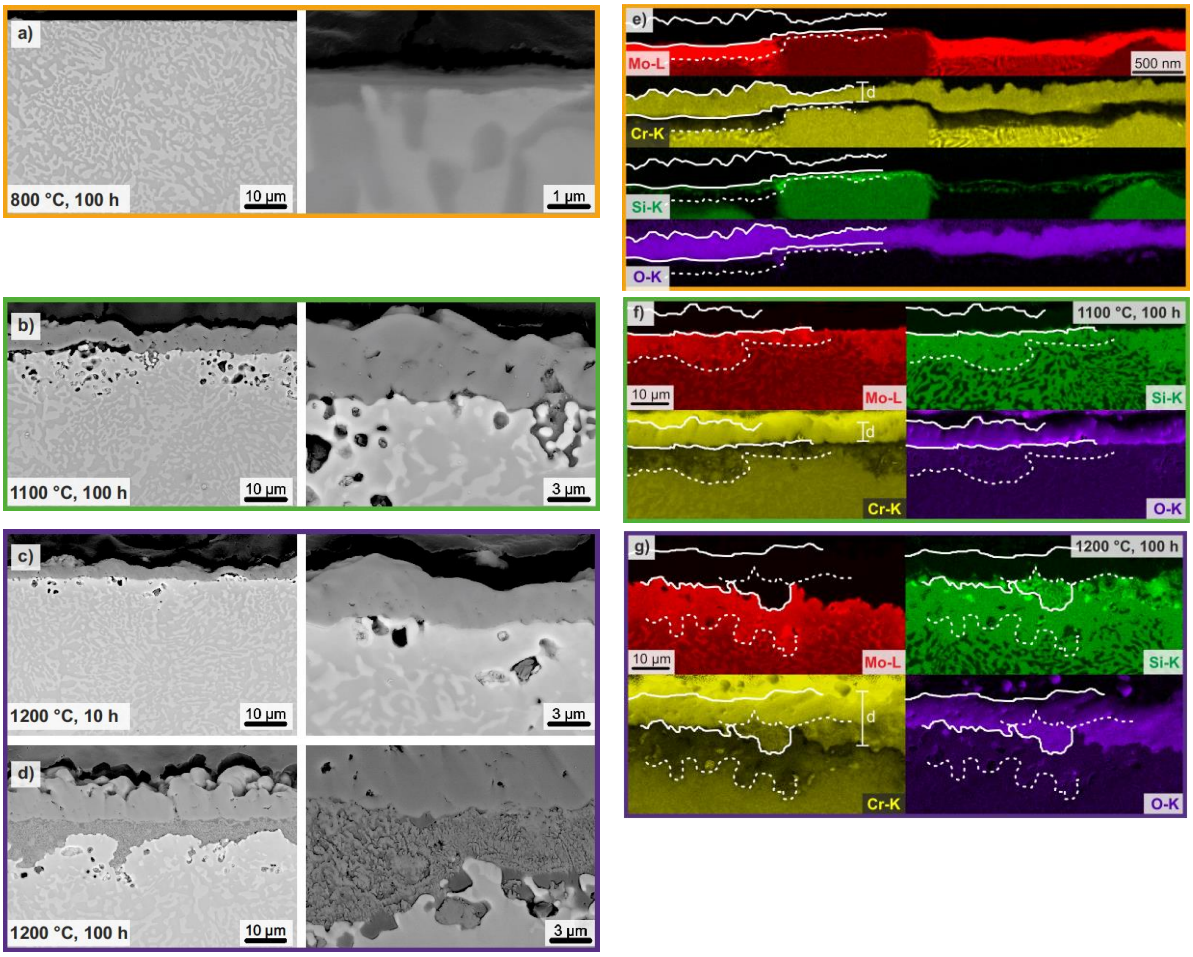

Fig. 4: BSE micrographs of the oxide scales forming during 100 hours of cyclic oxidation at a) 800, b) 1100 and 1200 °C as well as after c) 10 and d) 100 h. Subscale porosity is seen in b)-d). e) STEM-EDS mapping of the oxide scales after 100 h cyclic oxidation at 800 °C. ZAF quantified SEM-EDS element mappings of the oxide scales after 100 h at f) 1100 and g) 1200 °C. Continuous white lines indicate the borders of the oxide scale, the dashed lines below indicate the Cr depleted region. In g), a dashed line is added to mark the internal corrosion.

Oxidation experiments at 800 °C reveal that the sample surface still appears metallic with a green tinge after 100 h. The mass gain of the three samples is very small and remains below 0.1 mg/cm^2 (Fig. 3b) after this period of time. Oxidation at 800 °C leads to an extremely thin continuous surface layer of less than 1 µm in thickness after 100 h (see Fig. 4a). There is no indication of internal oxidation. In the XRD analysis in Fig. 5a, not only α-Cr_2O_3 is identified but also $(Cr,Mo)_{ss}$ and $(Cr,Mo)_3Si$. The Bragg peaks of either phase are marked with dark blue diamonds $(Cr,Mo)_{ss}$ and red sqares $(Cr,Mo)_3Si$ in the diffraction pattern in Fig. 5a. Additionally, a second solid solution $(Cr,Mo)_{ss}$ with a lattice parameter *a* of 3.144 Å is identified. It is indicated by light blue triangles in the diffraction pattern. The recalculated Cr concentration of this Mo-rich subsurface solid solution is added to Fig. 2a. STEM-EDS element maps confirm a Mo-rich, Cr-depleted, subsurface layer. Additionally, an extremely thin Si oxide layer formation is observed at the interface between bulk material and Cr_2O_3. The former homogeneous solid solution obviously decomposes into a Mo-rich and Cr-rich solid solution with a lamellar or stripe-like microstructure. This was observed in TEM close to the surface but also for regions deeper in the substrate (not shown here) after cyclic oxidation at 800 °C.

At 1100 °C, the sample surface appears dark and rough after 100 h, as seen in Fig. 3a but no spallation of the oxide scale is observed. Mass gain of all three samples tested is in the same order of magnitude. It is less than 1.5 mg/cm^2 after 100 h. From the BSE micrograph in Fig. 4b, it can be concluded that a continuous surface layer of about (4.8 ± 1.4) µm is formed. Furthermore, the formation of pores below the outer scale is observed but there is still no indication of internal oxidation similar to oxidation at 800 °C. The presence of α-Cr_2O_3, a solid solution $(Cr,Mo)_{ss}$ with a = 3.144 Å and a silicide phase $(Cr,Mo)_3Si$ with a = 4.865 Å is obtained from XRD. The oxide scale formed at 1100 °C consists solely of Cr and O. Mo and Si are detected predominantly in the substrate's microstructure with a sharp boundary to the oxide regions. A significant Cr depletion below the outer oxide scale is obtained. Mo and Si are enriched in this region. The partitioning of Si to solid solution and silicide vanishes and Si is distributed homogeneously in the Cr-depleted region.

Samples, which were oxidized for 100 h at 1200 °C, present a dark rough surface with a similar macroscopic appearance as for 1100 °C. Again, no spallation is observed up to 100 h of oxidation. As shown in Fig. 3d, mass gain is observed until 50 h of oxidation time, followed by a mass loss for the next 30 h, succeeded by only very small overall mass changes are measured after 80 h until 100 h of oxidation time. Figs. 4c and d show BSE images of the scales forming at 1200 °C after 10 h and 100 h, respectively. After 10 h, there is a continuous oxide scale of uniform thickness of (3.4 ± 0.9) µm. After 100 h, pronounced internal corrosion appears below the surface layer. The surface layer has a thickness of (7.9 ± 2.0) µm. As shown in Fig. 4d, the depth of the internal corrosion varies strongly with a median thickness of (6.6 ± 2.8) µm. Below the internal corrosion region the two-phase microstructure disappears and pores have formed. The only phase identified by XRD is α-Cr_2O_3. The SEM-EDS mappings depicted in Fig. 4f show the distinct difference between the chemical composition of the outer oxide layer and the region of internal corrosion. The specimen surface and the boundary between the scale and the substrate are indicated with continuous white lines. The dashed white lines in the scale mark the boundary between the chromia scale and the Si-enriched oxide region, potentially being an internal corrosion region. Again, the outer chromia scale contains neither Mo nor Si and the XRD analysis (see Fig. 5c) confirms the formation of Cr_2O_3. No other crystal structures are detected.

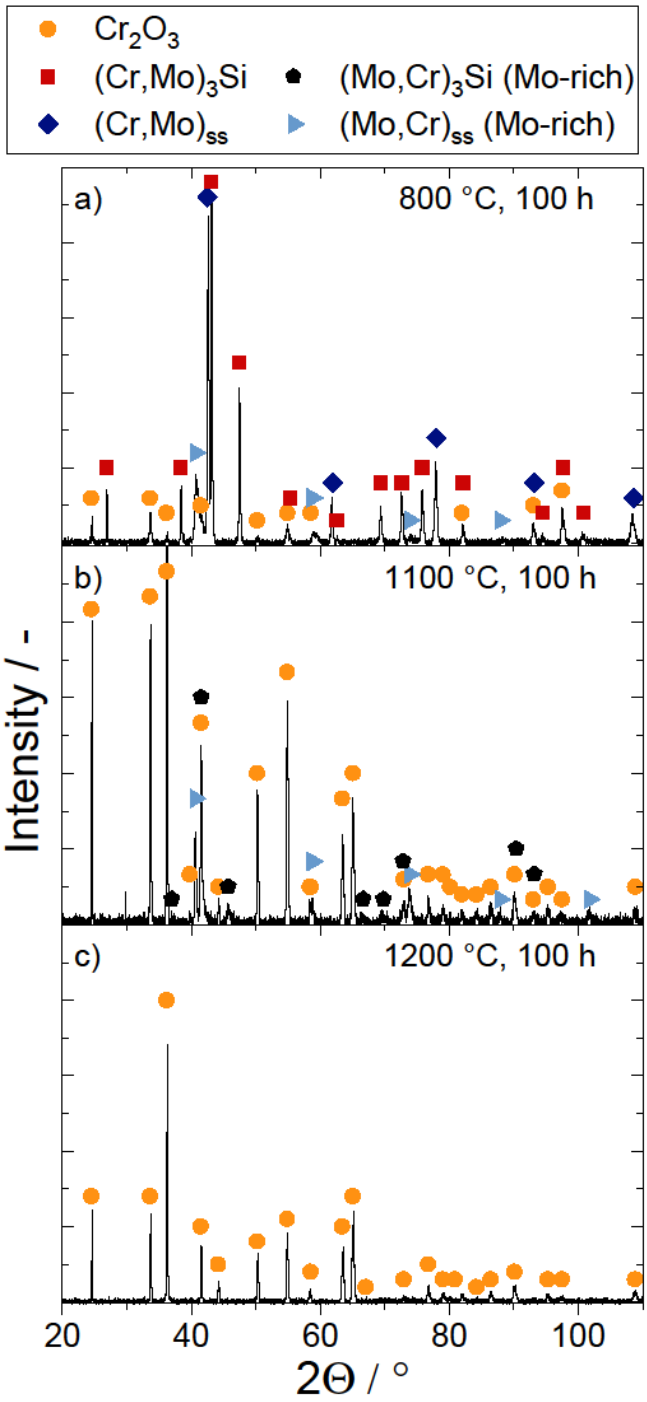

Fig. 5: Diffraction patterns of the oxide scales formed on the samples after 100 h of cyclic oxidation.

4 Discussion

4.1 Synthesis and microstructure

Analysis of the AC and HT microstructures showed that it is possible to synthesize monolithic σ phase via arc melting. A full decomposition into $(Cr,Mo)_{ss}$ and $(Cr,Mo)_3Si$ is achieved through a heat treatment, despite the dendritic AC microstructure. In the HT microstructure, there is no pronounced difference of Cr contents in the two phases. According to STEM-EDS analysis, the difference in Cr contents between the A2 and A15 phase in HT condition are only about 5 at.%. Therefore, Cr is equally available for the formation of a chromia layer from both phases and can prevent site-specific oxidation

of the Mo containing A2 phase in cyclic oxidation at 800 °C. In this respect, the situation is different from pesting-resistant Mo-Si-Ti alloys which exhibit significant difference in Ti and Si content and oxidize to TiO_2 and SiO_2 mixed oxide scales.

There are only incomplete assessments of the ternary Cr-Mo-Si phase diagram available in literature, for example in Ref. [31]. Information on the σ phase therein is limited basically to the report by Rudy and Nowotny [22]. Based on the reported solubility and stability ranges of binary $(Cr,Si)_{ss}$ (6.7 at.% Si [32]) and $(Mo,Si)_{ss}$ (0.3 at.% Si [33]) as well as Mo_3Si (~24 at.% [34]) and Cr_3Si (22.9 to 25.6 at.% [32]) at 1200 °C, Fig. 6 was constructed using data from the present study and the literature data. The binary limits at 1200 °C were linearly interpolated although Ref. [31] suggests a slightly concave shape at least for the solid solution at 1300 °C. Note that the present results extend the reported information on the σ phase from Ref. [22] with respect to: (i) slightly higher possible Cr contents (than for the suggested stability range at 1500 °C of Cr-(47-29)Mo-14Si in Ref. [22][1]), (ii) larger stability range of Si contents (ditto) and (iii) most importantly, the formation of the σ phase from the liquid in the Mo-Si-Cr system (as unknown so far [31], since Ref. [22] only reported on microstructures after long-term annealing treatments). The compositions of the solid solution and silicide phase after complete decomposition at 1200 °C are included as well. There is a slight deviation of the experimentally obtained composition ranges and the tie line connecting the phase compositions of $(Cr,Mo)_{ss}$ and $(Cr,Mo)_3Si$ across the nominal composition of the alloy after long-term annealing (expected to be an almost vertical tie line in Fig. 6). This might be probably due to an underestimation of the Cr content in the solid solution by the applied methods in this study and the still inhomogeneous Cr distribution following the dendritic solidification of the σ phase that was not removed by the 1200 °C annealing.

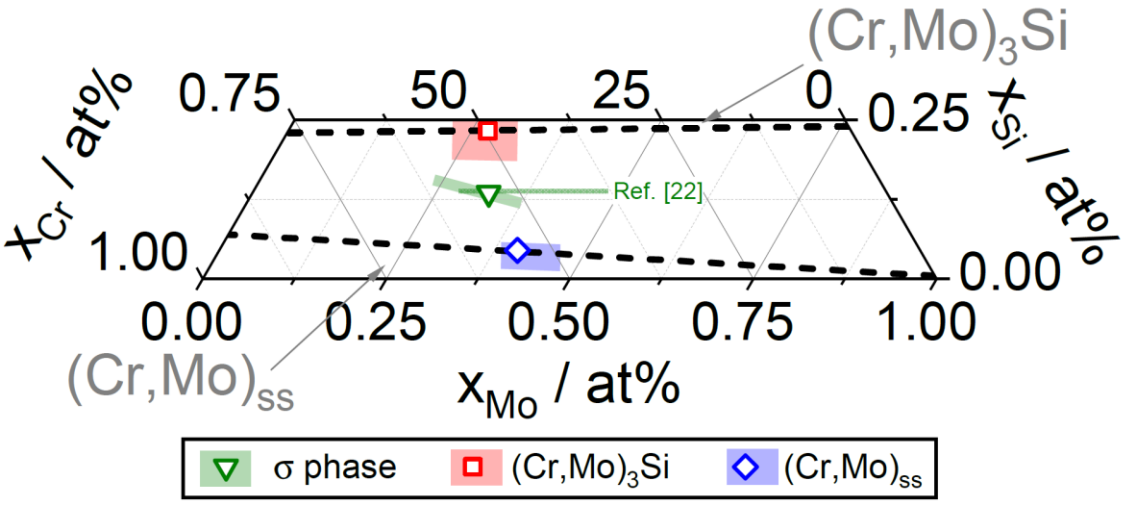

Fig. 6: Summary of the gained phase stability information. A monolithic σ phase is obtained for the nominal composition indicated by the triangle. The green shaded region indicates the range of compositions obtained in the dendritic AC microstructure. The proposed stability range of the σ phase at 1500 °C taken from Ref. [22] is included for comparison. The two-phase microstructure of $(Cr,Mo)_{ss}$ and $(Cr,Mo)_3Si$ is obtained after prolonged annealing at 1200 °C. The shaded regions indicate the composition ranges summarized in Tab. 1. Phase compositions of $(Cr,Mo)_{ss}$ and $(Cr,Mo)_3Si$ at 1200 °C were obtained by linear interpolation of the binary limits reported in literature.

[1] Note the wrong transfer of the reported stability range of the σ phase by Rudy and Nowotny [22] to Ref. [31].

The chemical compositions obtained by SEM and STEM-EDS analysis in general, listed in Tab. 1, deviate from the re-calculated Cr and Mo content via NR analysis. In case of SEM-EDS, the discrepancy originates from the fine-lamellar microstructure and comparably large probe size. It is likely that the probe volume includes both phases. The lamella for STEM-EDS however, only represents a very small, selected sample volume. As seen in Figs. 1a and b, the dendritic microstructure from AC is still present in the HT condition. The dendrites can still be obtained in the overview micrograph of the HT state and, thus, the STEM-EDS result represents information from the Cr depleted regions.

Apart from the successful synthesis of the desired fine-scaled, two-phase microstructure, two major issues are identified with respect to sample manufacturing and conditioning, that are:

(i) Incomplete decomposition of the σ phase during the heat treatment might be obtained depending on the dendrite size. In case of increased ingot size for the alloy, longer heat treatment durations might be needed to ensure complete decomposition (progressing from interdendritic regions into the dendrite centers) of widely spaced dendrites which result from slower cooling rates.

(ii) Pronounced cracking occurs in the σ phase already in the AC bulk material, which will affect mechanical properties and oxidation resistance upon cycling of large batches.

4.2 Oxide scales

The very small mass changes in Fig. 3b indicate a very good oxidation resistance at 800 °C. The origin of the initial mass changes up until 20 h of cyclic oxidation has yet to be determined. In the presence of Mo, low mass change might also result from a superposition of mass gain and simultaneous evaporation of MoO_3, which is usually formed at temperatures above 500 °C and potentially leads to the so-called pesting phenomenon. However, the scale thickness of less than 1 µm after 100 h at 800 °C is comparably low, which is consistent with the low mass gain and further indicates the absence of any evaporation. For pesting-resistant Mo-Si-Ti alloys, layer thicknesses of 2.3-5 µm are reported for those conditions [28,35]. Scale thicknesses of pure Cr, Cr-10Ni (wt.%) and Cr-10Fe (wt.%) have been reported to lie between 2-3 µm after only 10 h of cyclic oxidation at 800 °C [36].

From the XRD analysis of the oxide scale after 100 h at 800 °C, shown in Fig. 5a, Bragg peaks of the substrate phases are still obtained due to the thin oxide scale. It is found that two different A2 as well as A15 phases exist in the subsurface region after oxidation (compare different lattice parameters shown in Fig. 2). In these regions, Cr and Mo concentrations were determined using XRD in combination with NR and set into ratio. A Mo:Cr ratio of 99:1 was found for the A2 phase formed during oxidation while the phase has a ratio of 44:56 in the HT condition. This can be explained by an outward diffusion of Cr towards the surface to form the Cr_2O_3 layer and hereby leading to a Mo enrichment in the subsurface zone. Due to the verification of Mo enrichment, an evaporation of MoO_3 can be excluded. The Mo enrichment appears to be more pronounced at the interface between $(Cr,Mo)_{ss}$ and Cr_2O_3 layer, than between $(Cr,Mo)_3Si$ and Cr_2O_3. Si oxide formation however, is more pronounced on top of $(Cr,Mo)_3Si$, due to the availability of Si from that phase. Our observations agree with the suggestions made in Ref. [16], that Si oxide acts as a barrier for Cr outward diffusion and reduces the driving force for inward diffusion of O through the scale due to the higher O content of SiO_2 compared to Cr_2O_3. Elemental maps of Mo and Cr show a lamellar structure in $(Cr,Mo)_{ss}$ in the transition region to the Cr depletion due to the miscibility gap suggested in binary Cr-Mo and the prolonged duration of cycling between room temperature and 800 °C [37,38]. It is concluded that a thin, protective chromia scale forms on Cr-13.5Si-32.2Mo at 800 °C, which makes the alloy pesting-resistant. A schematic scale mockup is depicted in Fig. 7a.

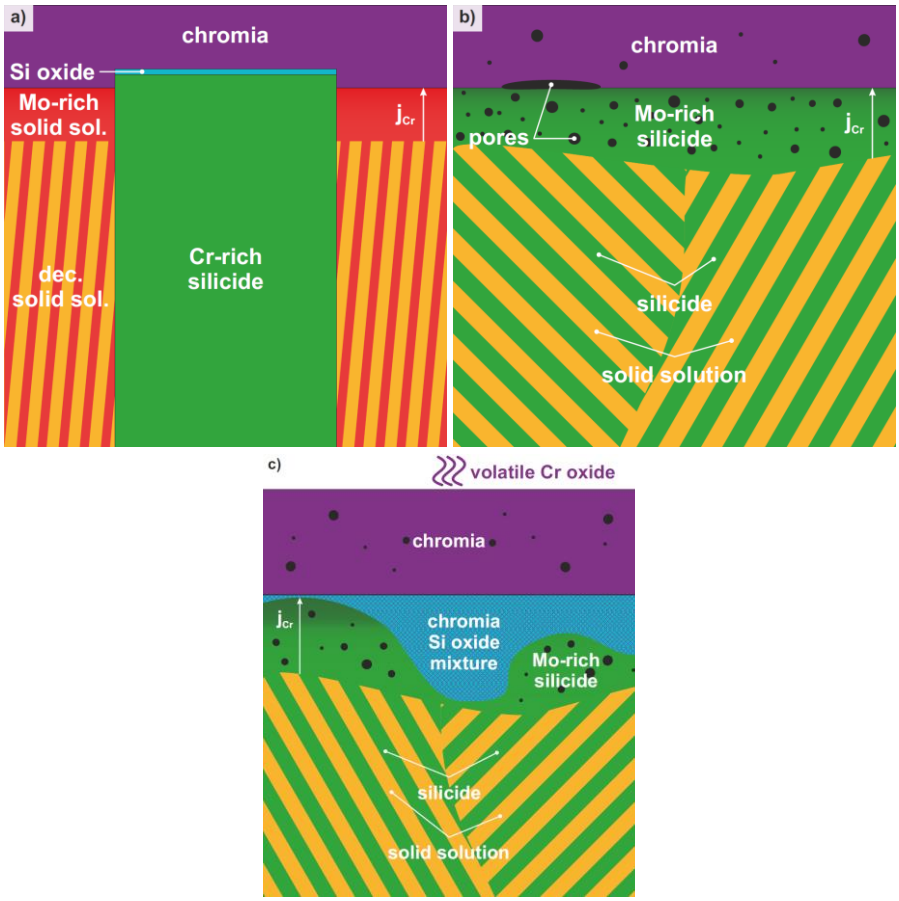

Fig. 7: Schematic of the scale mockup and oxidation mechanisms during long-term oxidation obtained from the present investigation: a) 800, b) 1100 and c) 1200 °C.

At 1100 °C, layer thicknesses are again lower than in pesting-resistant Mo-Si-Ti alloys with 0.5, 3 and 5 µm (Cr-13.5Si-32.2Mo) versus 5, 13, 26 µm (Mo-20Si-52.8Ti) for 1, 10 and 100 h of oxidation time, respectively, under the same oxidation conditions. For Ni-32.6Cr, a 12.5 µm chromia scale is reported after 50 h of isothermal oxidation in Ref. [39], whereas Ref. [36] reports 17 and 20 µm scale thicknesses after 10 h of cyclic oxidation of Cr and Cr-10Fe (wt.%) at 1100 °C, respectively. The Cr_2O_3 scale and the elemental distribution below the oxide scale are indicative of Cr outward diffusion and formation of a protective scale, effectively suppressing evaporation of MoO_3. Subsurface A2 and A15, still detected in the XRD patterns through the oxide scales, are both significantly depleted in Cr in agreement with the SEM-EDS maps. Taking the low solubility of Si in $(Cr,Mo)_{ss}$ (1100 °C up to 5 at.% in equilibrium) into account, the SEM-EDS maps reveal that the increasing Si content in the subsurface region leads to a decreasing, partially even disappearing, volume fraction of the solid solution phase, in favor of a A15 subsurface region. The transformation from the dual-phase initial microstructure to the A15 subsurface region results in the formation of significant porosity in that region. The compositions and lattice parameters of the constituting phases in Tab. 1 and Fig. 2, respectively, indicate crystallographic densities in the initial condition of 8.7 and 7.8 g/cm³ for $(Cr,Mo)_{ss}$ and $(Cr,Mo)_3Si$, respectively. Hence, the alloy exhibits a density of approximately 8.2 g/cm³ given the volume fractions of the constituting phases. The monolithic A15 subsurface region instead would yield a significantly increased density of 9.0 g/cm³ considering its lattice parameters and composition. Hence, a significant amount of free volume is needed to compensate this difference in densities. In conclusion, a scale mockup as schematically depicted in Fig. 7b is proposed which is dominated by the Cr depletion due to the Cr formation in the subsurface region.

Despite the mass loss after 50 h of cyclic oxidation, the samples oxidized at 1200 °C do not exhibit significant spallation. The layer thickness of 15 µm after 100 h is in the same range as oxide scales measured in Ref. [16] for Cr-Si alloys. 15-22 µm thick scales were formed on Cr-7Si-2X (X=Ge, Pt, Mo) after 100 h in these isothermal oxidation experiments at 1200 °C under synthetic air. Since no crystal structures other than α-Cr_2O_3 chromia were the detected, Si-enriched oxide regions might be oxidized to amorphous SiO_2.

A significant Cr depletion zone is detected below the scale. This is indicated by the dashed line within the substrate in Fig. 4f. From the BSE image in Fig. 4c (larger magnification on the right side), it can be concluded that no internal corrosion is present after 10 h. In contrast, significant internal corrosion takes place between 10 and 100 h of oxidation at 1200 °C. Hence, the initial protection by chromia formation gets lost. Paths through the oxide scale can be seen in the chromia scale in Fig. 4d, which can allow O inward diffusion. The progression of the mass change indicate, that up until 50 h Cr_2O_3 formation is dominant in mass change kinetics. After 50 h, evaporation becomes dominant over scale formation, leading to net mass losses. It is reasonable that Cr_2O_3 is the evaporating species rather than MoO_3. In the surface layer, no Mo was detected (see Fig. 4f) and low O partial pressure in the Cr depleted region of the bulk makes the formation of MoO_3 unlikely. The very low mass changes after 80 h suggest, that evaporation processes terminated or got balanced to equal extent. The progress of oxidation after the transient stage might be visualized as shown in Fig. 7c. The situation is dominated by the evaporation of the volatile species and the significant internal corrosion.

During all oxidation experiments performed in this study, no nitride formation is found in any of the investigated specimens. The formation of brittle Cr_2N during exposure needs to be considered the most important challenges for development of oxidation-resistant, Cr-based alloys [11,40–42]. In terms of mass gain and the determination of mass gain kinetics the formation of Cr_2N results in even thicker scales and therefore higher mass gains in comparison to the oxide formation [43]. For example, after isothermal oxidation of pure Cr at 1200 °C in synthetic air, a Cr_2O_3 scale thickness of 66 µm was measured in comparison to an additional 352 µm of Cr_2N [16]. Alloying Cr with Si improves its resistance as the A15 phase is intrinsically resistant against nitridation which was proven by thermodynamic calculations as well as experiments [14]. Cr-Si alloys, consisting of both A2 solid solution as well as A15 silicide phase, only show Cr_2N formation in the regions of former Cr_{ss} which is detrimental for mechanical properties [44]. Nitride formation was recently attributed to Cr_2O_3 scale failure and oxide scale cracking rather than atomic diffusion though the oxide scale [45]. The present results on Cr-13.5Si-32.2Mo might be rationalized by the changes of the subsurface microstructure as depicted in Figs. 4e and f. The Cr depletion as well as Mo and Si enrichment leads to an almost single-phase A15 silicide region which might prevent and shield the two-phase substrate material from nitridation. As reported in Ref. [46], additions of Mo to $(Cr,Mo)_{ss}$ – the threshold is expected between 5–8 at.% – further increase the resistance of the A2 phase towards nitridation [46]. This is in agreement with the present observations as the investigated alloy contains around 32 at.% Mo without distinct portioning to the individual phases.

To summarize, the alloy Cr-13.5Si-32.2Mo behaves differently at each of the temperatures tested. Whereas 800 °C lies comfortably below critical temperatures for the formation of volatile Cr species, 1100 °C is already critical for many Cr rich alloys due to evaporation and nitridation. Inward diffusion of N was *not* found at any temperature in the present study. For this temperature, mass gain and scale thickness both point towards a parabolic oxidation rate and the formation of protective chromia. At 1200 °C, the alloy suffers from internal corrosion for longer periods of exposure.

4.3 Oxidation kinetics

For the dependence of the oxide scale thickness d over the exposure time t, the power law function

$$d^n = k_{d,n} \cdot t \quad (1)$$

was applied. $k_{d,n}$ is the growth rate constant related to the scale thickness. The exponent n was once adjusted individually to achieve optimum fit quality as indicated by the dashed lines in Fig. 8. For scale measurement a conservative error estimation was used. For 1200 °C, the double layer was considered for scale measurement. Statistical fluctuations are taken into account in the fits. For further calculations error propagation was considered.

For 800 °C and 1100 °C, $k_{d,n}$ was additionally calculated with n being fixed to 2, which corresponds to a (true) parabolic growth law [47]. The calculated values for $k_{d,n}$ with variable and fixed n are listed in Tab. 2 including the fit quality R^2_{adj}.

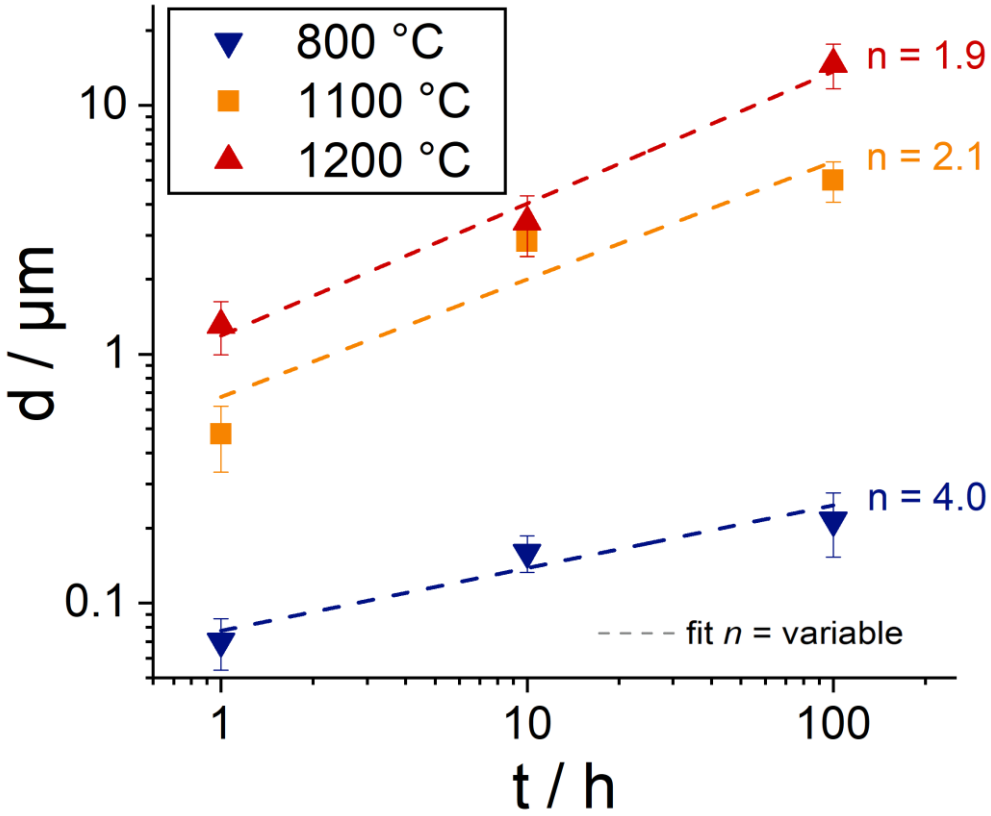

Fig. 8: Oxide scale thicknesses d of Cr-13.5Si-32.2Mo with growth exponent n fitted according to Eq. (1) For samples oxidized 800 °C, and 1100 °C the scale was considered to solely consist of the Cr_2O_3 layer observed in BSE and EDS. At 1200 °C additionally the internal oxidation was considered.

However, often the oxidation progress is obtained from mass gain over time [48]:

$$\left(\frac{\Delta m}{A}\right)^n = k_{m,n} \cdot t \tag{2}$$

with the mass change Δm, the specimen surface area A and the oxidation rate constant $k_{m,n}$. To conclude parabolic oxidation from a mass change curves, additional information on the oxide scale needs to be obtained. For parabolic oxidation, the substrate degradation is slowed down over time by the formation of a protective scale. Since the weight change could be influenced by evaporating species, mass changes could appear to be parabolic but scale growth might not, due to an equilibrium of formation and evaporation.

Tab. 2. Growth or oxidation rate constants $k_{d,n}$ or $k_{m,n}$ for 800, 1100 and 1200 °C. Note that for fitting data of one sample in Fig. 3c, a constant offset was assumed for the determination of the parabolic fit of mass gain. $k^*_{d,n}$ marked with * was converted from the averaged oxidation constant $k_{m,n}$ using Eq. (4).

T / °C	fit for	constant	unit	n / 1	value of k	R^2_{adj} / 1
800	thickness	$k_{d,n}$	$cm^n\ s^{-1}$	3.96	$1.43 \cdot 10^{-24}$	0.81
				4	$1.01 \cdot 10^{-24}$	0.91
1100	thickness	$k_{d,n}$	$cm^n\ s^{-1}$	2.11	$4.19 \cdot 10^{-13}$	0.71
				2	$1.08 \cdot 10^{-12}$	0.85
	thickness*	$k^*_{d,n}$	$cm^n\ s^{-1}$	2	$1.09 \cdot 10^{-12}$	–
	mass change	$k_{m,n}$	$g^n\ cm^{-2n}\ s^{-1}$	2.30–5.37	–	> 0.99
				2	$2.97 \cdot 10^{-12}$	0.82–0.98
1200	thickness	$k_{d,n}$	$cm^n\ s^{-1}$	1.88	$1.11 \cdot 10^{-11}$	0.94
				2	$4.55 \cdot 10^{-12}$	0.96

For 800 °C, $k_{d,n}$ yields a quartic growth with $n = 4$ with reasonable R^2_{adj}. For 1100 and 1200 °C, fits to the progression of the scale thickness resulted in n values close to 2. Therefore, the scale thicknesses at 1100 and 1200 °C follow parabolic growth laws with very good fit quality. However, considering the mass changes (see Figs. 3b-d), only the oxidation behavior at 1100 °C might actually qualify as parabolic since significant mass loss occurs beyond 50 h at 1200 °C indicative of evaporation.

In Fig. 9, parabolic growth constants $k_{d,n=2}$ and mass change constants $k_{m,n=2}$ of several chromia forming materials from literature [14,16,36,39,49] as well as the Mo-20Si-52.8Ti reference alloy [35] are plotted for oxidation temperatures between 800 and 1300 °C in an Arrhenius-type diagram. The dashed lines solely connect $k_{d,n=2}$ data points from one and the same study and only serve as guides to the eye. Parabolic growth rates $k_{d,n=2}$ of Cr-13.5Si-32.2Mo were obtained for 1100 and 1200 °C and included in Fig. 9. Data for 800 °C is omitted due to the quartic growth law. Filled symbols represent studies with direct scale thickness measurements. Data with half-filled symbols are taken from studies where $k_{m,n=2}$ were determined by mass gain measurements. $k^*_{d,n}$ values were approximated assuming that mass change is caused exclusively by inwards diffusion of O forming solid, monolithic Cr_2O_3 and no species were evaporating. Combining Eqs. (1) and (2) under these conditions yields:

$$k^*_{d,n} = k_{m,n}\left(\frac{d \cdot A}{\Delta m}\right)^n \tag{3}$$

The mass gain Δm by solid oxide formation, using the amount of substance n and molar masses M, is $\Delta m = n_{\mathrm{O\ in\ Cr_2O_3}}\, M_\mathrm{O} = 3\, n_{\mathrm{Cr_2O_3}}\, M_\mathrm{O} = 3\frac{M_\mathrm{O}}{M_{\mathrm{Cr_2O_3}}} m_{\mathrm{Cr_2O_3}}$. The mass of Cr_2O_3 $m_{\mathrm{Cr_2O_3}}$ is obtained from

its density $\rho_{Cr_2O_3}$ and estimated using its thickness d and the surface area of the specimen A as $m_{Cr_2O_3} = \rho_{Cr_2O_3} \cdot V_{Cr_2O_3} \approx \rho_{Cr_2O_3} \cdot d \cdot A$, with $V_{Cr_2O_3}$ being the volume of the chromia scale. Hence, the following relationship is obtained:

$$k^*_{d,n} = k_{m,n} \left(\frac{M_{Cr_2O_3}}{\rho_{Cr_2O_3} \cdot 3\, M_O} \right)^n \quad (4)$$

The parabolic growth constants $k^*_{d,n=2}$, plotted in Fig. 9a were recalculated the with $M_{Cr_2O_3} = 152\ \mathrm{g/mol}$, $M_O = 16\ \mathrm{g/mol}$ and $\rho_{Cr_2O_3} = 5.2\ \mathrm{g/cm^3}$. The green semi-filled symbols in Fig. 9 are representative of an oxidation study where the Si content was systematically varied between pure Cr and Cr-25Si [14]. The positive influence of increasing Si on the oxidation and growth rates is obvious from the diagram. The calculated growth constants of pure Cr from Refs. [14] and [16] at 1200 °C are rather high as compared to an extrapolation of experimental $k_{d,n=2}$ values from Ref. [36]. However, these $k^*_{d,n=2}$ values obtained from literature by conversion of $k_{m,n=2}$ might still underestimate the progression of the oxidation, since evaporation effects are neglected in the calculation. It should also be noticed that the calculated $k^*_{d,n=2}$ of pure Cr from Ref. [14] lies more than one order of magnitude above the calculated $k^*_{d,n=2}$ of Cr-Si alloys of the same study, showing the positive influence of Si. Spallation, evaporation and nitridation of Cr_2O_3 scales at high temperatures complicates the determination of $k_{m,n}$. In isothermal experiments as e.g. in Ref. [16], the parabolic rate constants are often obtained until the first rapid mass gain, before scale spallation. If scale spallation is observed, $k_{m,n=2}$ would likely be much higher than directly obtained $k_{d,n=2}$. This must be especially considered when comparing results from isothermal oxidation to cyclic oxidation as in Fig. 9. Among the chosen chromia-forming alloys, $k_{d,n=2}$ roughly lies at about 10^{-10} $cm^2\ s^{-1}$. Cr-13.5Si-32.2Mo with $k_{d,n=2}$ of $1.08 \cdot 10^{-12}$ and $4.55 \cdot 10^{-12}$ $cm^2\ s^{-1}$ for 1100 and 1200 °C, respectively, comfortably lies more than one order of magnitude below that. An almost perfect agreement of the conversion from $k_{m,n=2}$ to $k^*_{d,n=2} = 1.09 \cdot 10^{-12}$ $cm^2\ s^{-1}$ and the directly obtained $k_{d,n=2}$ is obtained for 1100 °C. This is considered proof, that there is no significant evaporation, internal oxidation or nitridation. The oxidation scale appears to be solely formed of solid Cr_2O_3 on Cr-13.5Si-32.2Mo at 1100 °C. A direct comparison of the experimentally determined mass change and hypothetic mass changes based on the formation of solid, monolithic Cr_2O_3 from the thickness measurements is included in the Supplementary material Fig. S1 for all temperatures tested. A positive influence of small Mo additions to Cr-Si alloys regarding the decrease in the formation of volatile species was observed by Ulrich et al. [16] for Cr-7Si-2Mo. The results for Cr-13.5Si-32.2Mo support these observations and extend the statement to much higher Mo contents. Up to 100 h of oxidation, the novel Cr-13.5Si-32.2Mo alloy overall possesses excellent oxidation behavior compared to a variety of chromia formers and – due to their pesting failure – to most Mo alloys containing large amount of Mo-rich solid solution.

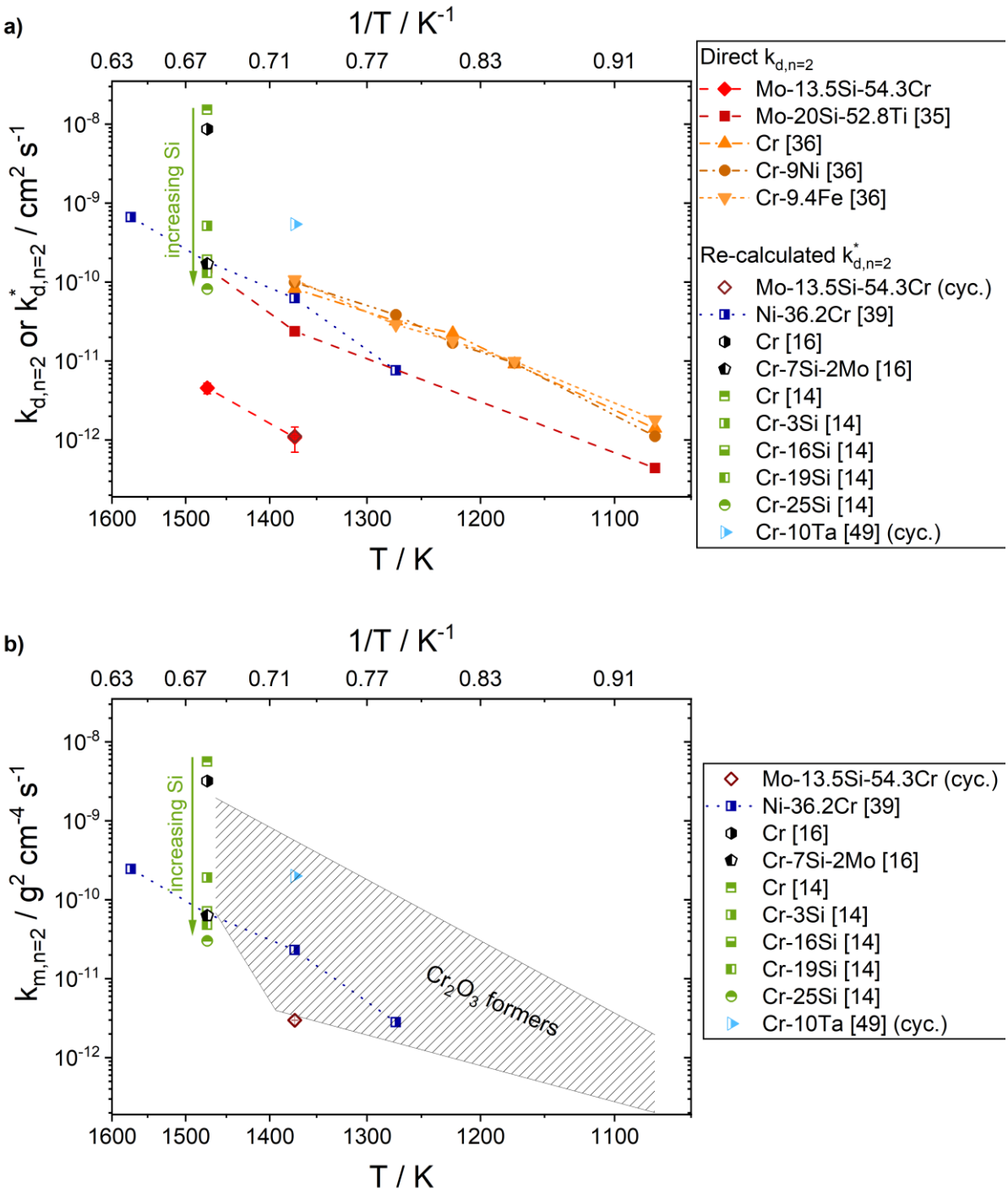

Fig. 9: a) Oxidation rate constants $k_{d,n=2}$ for parabolic scale growth of several Cr_2O_3 formers [14,16,36,39,49] reported in literature and of the eutectic Mo-Si-Ti reference alloy from Ref. [35]. Data obtained by mass gain (indicated by semi-filled symbols) were converted using Eq. (4). b) Mass change constants $k_{m,n=2}$ for parabolic scale growth of several Cr_2O_3 formers [14,16,39,49] reported in literature. All direct $k_{d,n=2}$ are obtained from cyclic oxidation experiments. Re-calculated $k^*_{d,n=2}$ as well as $k_{m,n=2}$ are obtained from isothermal oxidation experiments unless otherwise indicated by (cyc.).

4.4 Potential application

In order to benefit from the oxidation resistance of Cr-13.5Si-32.2Mo in a potential application, the manufacturing is presently limited due to the presence of the σ phase during synthesis. This might be avoided by the application of a bottom-up processing of mechanically alloyed powders and the direct synthesis of the two-phase microstructure from a super-saturated condition. Another approach might envisage alloys free of or lean in σ phase as Cr, the major element contributing to the oxidation resistance, is rather homogeneously distributed across the solid solution and silicide. Hence, lower Si contents might also lead to outstanding oxidation resistance but also to much larger fractions of potentially ductile solid solution.

5 Conclusions

The following conclusions can be drawn from the present study and the discussion of its results:

- A metastable, monolithic σ phase in the Mo-Si-Cr system is obtained for Cr-13.5Si-32.2Mo (at.%) from the liquid. It fully decomposes into a fine-lamellar microstructure of solid solution $(Cr,Mo)_{ss}$ and $(Cr,Mo)_3Si$ (Cr_3Si prototype) through a solid state reaction with only marginally difference in Cr contents.
- Cyclic oxidation in laboratory air shows outstanding oxidation resistance by the formation of chromia scales with small mass gain at 800 and 1100 °C for up to 100 h. Chromia formation leads to Mo and Si enrichment in the subsurface region and the formation of a Mo-rich $(Cr,Mo)_3Si$ region that prevents the material from nitridation.
- Good oxidation behavior is noted at 1200 °C. However, internal oxidation and evaporation of Cr_2O_3 is obtained at this temperature beyond 50 h.
- No scale spallation occurred for any of the temperatures tested.
- Oxidation rate constants associated with quartic and parabolic rate laws at 800 and 1100 °C, respectively, are very low compared to other Cr_2O_3 formers.

6 Acknowledgements

We gratefully acknowledge financial support by the Deutsche Forschungsgemeinschaft (DFG) within the framework of GRK 2561 MatCom-ComMat. This work was partly carried out with the support of the Karlsruhe Nano Micro Facility (KNMFi, www.knmf.kit.edu), a Helmholtz Research Infrastructure at Karlsruhe Institute of Technology (KIT, www.kit.edu).

7 Data availability statement

The raw data required to reproduce these findings are available on request to alexander.kauffmann@kit.edu. The processed data required to reproduce these findings are available on request to alexander.kauffmann@kit.edu.

8 References

[1] J.H. Perepezko, M. Krüger, M. Heilmaier, Mo-Silicide Alloys for High-Temperature Structural Applications, Matls. Perf. Charact. 10 (2021). https://doi.org/10.1520/MPC20200183.

[2] D. Schliephake, A. Kauffmann, X. Cong, C. Gombola, M. Azim, B. Gorr, H.-J. Christ, M. Heilmaier, Constitution, oxidation and creep of eutectic and eutectoid Mo-Si-Ti alloys, Intermetallics 104 (2019) 133–142. https://doi.org/10.1016/j.intermet.2018.10.028.

[3] S. Obert, A. Kauffmann, S. Seils, S. Schellert, M. Weber, B. Gorr, H.-J. Christ, M. Heilmaier, On the chemical and microstructural requirements for the pesting-resistance of Mo–Si–Ti alloys, J. Mater. Res. Technol. 9 (2020) 8556–8567. https://doi.org/10.1016/j.jmrt.2020.06.002.
[4] S. Obert, A. Kauffmann, M. Heilmaier, Characterisation of the oxidation and creep behaviour of novel Mo-Si-Ti alloys, Acta Mater. 184 (2020) 132–142. https://doi.org/10.1016/j.actamat.2019.11.045.
[5] J. Unnam, R.N. Shenoy, R.K. Clark, Oxidation of commercial purity titanium, Oxid. Met. 26 (1986) 231–252. https://doi.org/10.1007/BF00659186.
[6] M. Yoshihara, Y.-W. Kim, Oxidation behavior of gamma alloys designed for high temperature applications, Intermetallics 13 (2005) 952–958. https://doi.org/10.1016/j.intermet.2004.12.007.
[7] J. Dai, J. Zhu, C. Chen, F. Weng, High temperature oxidation behavior and research status of modifications on improving high temperature oxidation resistance of titanium alloys and titanium aluminides: A review, J. Alloys Compd. 685 (2016) 784–798. https://doi.org/10.1016/j.jallcom.2016.06.212.
[8] W. Trzebiatowski, H. Ploszek, J. Lobzowski, X-Ray Analysis of Chromium-Molybdenum and Chromium-Tungsten Alloys, Anal. Chem. 19 (1947) 93–95. https://doi.org/10.1021/ac60002a006.
[9] I.H. Kim, H.S. Oh, S.J. Kim, E.S. Park, Rapid assessment of solid solution hardening via atomic size misfit parameter in refractory concentrated alloys, J. Alloys Compd. 886 (2021) 161320. https://doi.org/10.1016/j.jallcom.2021.161320.
[10] H. Nowotny, H. Schroth, R. Kieffer, F. Benesovsky, Der Aufbau einiger Silizidsysteme von Übergangsmetallen, Monatsh. Chem. 84 (1953) 579–584. https://doi.org/10.1007/BF00900790.
[11] A.S. Dorcheh, M.C. Galetz, Challenges in Developing Oxidation-Resistant Chromium-Based Alloys for Applications Above 900°C, JOM 68 (2016) 2793–2802. https://doi.org/10.1007/s11837-016-2079-7.
[12] J.H. Perepezko, The Hotter the Engine the Better, Science 326 (2009) 1067–1068. https://doi.org/10.1126/science.1179117.
[13] E.A. Gulbransen, K.F. Andrew, Kinetics of the Oxidation of Chromium, J. Electrochem. Soc. 104 (1957) 334–338.
[14] A. Soleimani-Dorcheh, M.C. Galetz, Oxidation and Nitridation Behavior of Cr–Si Alloys in Air at 1473 K, Oxid. Met. 84 (2015) 73–90. https://doi.org/10.1007/s11085-015-9544-5.
[15] E.A. Gulbransen, K.F. Andrew, A Preliminary Study of the Oxidation and Vapor Pressure of Chromium, J. Electrochem. Soc. 99 (1952) 402. https://doi.org/10.1149/1.2779609.
[16] A.S. Ulrich, P. Pfizenmaier, A. Solimani, U. Glatzel, M.C. Galetz, Improving the oxidation resistance of Cr-Si-based alloys by ternary alloying, Corros. Sci. 165 (2020) 108376. https://doi.org/10.1016/j.corsci.2019.108376.
[17] L. Royer, X. Ledoux, S. Mathieu, P. Steinmetz, On the Oxidation and Nitridation of Chromium at 1300 °C, Oxid. Met. 74 (2010) 79–92. https://doi.org/10.1007/s11085-010-9198-2.
[18] H. Bei, E. George, E. Kenik, G. Pharr, Directional solidification and microstructures of near-eutectic Cr–Cr3Si alloys, Acta Mater. 51 (2003) 6241–6252. https://doi.org/10.1016/S1359-6454(03)00447-6.
[19] A. Tomasi, R. Ceccato, M. Nazmy, S. Gialanella, Microstructure and oxidation behaviour of chromium–molybdenum silicides, Mater. Sci. Eng., A 239-240 (1997) 877–881. https://doi.org/10.1016/S0921-5093(97)00678-3.

493 [20] S. Ochiai, Improvement of the oxidation-proof property and the scale structure of Mo3Si
494 intermetallic alloy through the addition of chromium and aluminum elements, Intermetallics 14
495 (2006) 1351–1357. https://doi.org/10.1016/j.intermet.2006.01.059.
496 [21] S.V. Raj, An evaluation of the properties of Cr3Si alloyed with Mo, Mater. Sci. Eng., A 201
497 (1995) 229–241. https://doi.org/10.1016/0921-5093(95)09767-8.
498 [22] E. Rudy, H. Nowotny, Eine sigma-Phase im System Chrom-Molybdän-Silicium, Monatsh.
499 Chem. (1974) 156–168.
500 [23] S. Burk, B. Gorr, V.B. Trindade, H.-J. Christ, Effect of Zr Addition on the High-Temperature
501 Oxidation Behaviour of Mo–Si–B Alloys, Oxid. Met. 73 (2010) 163–181.
502 https://doi.org/10.1007/s11085-009-9175-9.
503 [24] M.A. Azim, D. Schliephake, C. Hochmuth, B. Gorr, H.-J. Christ, U. Glatzel, M. Heilmaier, Creep
504 Resistance and Oxidation Behavior of Novel Mo-Si-B-Ti Alloys, JOM 67 (2015) 2621–2628.
505 https://doi.org/10.1007/s11837-015-1560-z.
506 [25] D. Caplan, G.I. Sproule, Effect of oxide grain structure on the high-temperature oxidation of Cr,
507 Oxid. Met. 9 (1975) 459–472. https://doi.org/10.1007/BF00611694.
508 [26] C.A. Schneider, W.S. Rasband, K.W. Eliceiri, NIH Image to ImageJ: 25 years of image analysis,
509 Nat Methods 9 (2012) 671–675. https://doi.org/10.1038/nmeth.2089.
510 [27] J.B. Nelson, D.P. Riley, An experimental investigation of extrapolation methods in the derivation
511 of accurate unit-cell dimensions of crystals, Proc. Phys. Soc. 57 (1945) 160–177.
512 [28] S. Obert, A. Kauffmann, R. Pretzler, D. Schliephake, F. Hinrichs, M. Heilmaier, The Creep and
513 Oxidation Behaviour of Pesting-Resistant (Mo,Ti)5Si3-Containing Eutectic-Eutectoid Mo-Si-Ti
514 Alloys, Metals 11 (2021) 169. https://doi.org/10.3390/met11010169.
515 [29] D. Sturm, M. Heilmaier, J.H. Schneibel, P. Jéhanno, B. Skrotzki, H. Saage, The influence of
516 silicon on the strength and fracture toughness of molybdenum, Mater. Sci. Eng., A 463 (2007)
517 107–114. https://doi.org/10.1016/j.msea.2006.07.153.
518 [30] H.J. Goldschmidt, J.A. Brand, The constitution of the chromium-niobium-silicon system, J. Less-
519 Common Met. 3 (1961) 34–43. https://doi.org/10.1016/0022-5088(61)90041-8.
520 [31] L. Pandelaers, R. Schmid-Fetzer (Eds.), Chromium – Molybdenum – Silicon, Landolt-Börnstein -
521 Group IV Physical Chemistry, 11E3, Springer-Verlag Berlin Heidelberg, 2010.
522 [32] B. Predel (Ed.), Cr - Si (Chromium - Silicon), Landolt-Börnstein - Group IV Physical Chemistry,
523 12B, Springer-Verlag Berlin Heidelberg, 2012.
524 [33] B. Predel (Ed.), Mo-Si (Molybdenum-Silicon), Landolt-Börnstein - Group IV Physical
525 Chemistry, 5H, Springer-Verlag Berlin Heidelberg, 1997.
526 [34] I. Rosales, J. Schneibel, Stoichiometry and mechanical properties of Mo3Si, Intermetallics 8
527 (2000) 885–889. https://doi.org/10.1016/S0966-9795(00)00058-3.
528 [35] S. Obert, A. Kauffmann, S. Seils, T. Boll, S. Kauffmann-Weiss, H. Chen, R. Anton, M.
529 Heilmaier, Microstructural and chemical constitution of the oxide scale formed on a pesting-
530 resistant Mo-Si-Ti alloy, Corros. Sci. 178 (2021) 109081.
531 https://doi.org/10.1016/j.corsci.2020.109081.
532 [36] K. Taneichi, T. Narushima, Y. Iguchi, C. Ouchi, Oxidation or Nitridation Behavior of Pure
533 Chromium and Chromium Alloys Containing 10 mass%Ni or Fe in Atmospheric Heating, Mater.
534 Trans. 47 (2006) 2540–2546. https://doi.org/10.2320/matertrans.47.2540.
535 [37] V. Jindal, B.N. Sarma, S. Lele, A thermodynamic assessment of the Cr–Mo system using CE-
536 CVM, Calphad 43 (2013) 80–85. https://doi.org/10.1016/j.calphad.2013.10.003.

[38] M. Venkatraman, J.P. Neumann, The Cr−Mo (Chromium-Molybdenum) system, in: G.D. Considine (Ed.), Van Nostrand's Encyclopedia of Chemistry, John Wiley & Sons, Inc, Hoboken, NJ, USA, 2005, pp. 216–220.
[39] P. Berthod, Kinetics of High Temperature Oxidation and Chromia Volatilization for a Binary Ni–Cr Alloy, Oxid. Met. 64 (2005) 235–252. https://doi.org/10.1007/s11085-005-6562-8.
[40] M.P. Brady, J.H. Zhu, C.T. Liu, P. Tortorelli, L.R. Walker, C.G. McKamey, J.L. Wright, C.A. Carmichael, D.J. Larson, M.K. Miller, W.D. Porter, Intermetallic reinforced Cr alloys for high-temperature use, Mater. High Temp. 16 (1999) 189–193. https://doi.org/10.1179/mht.1999.018.
[41] M.P. Brady, P.F. Tortorelli, L.R. Walker, Water Vapor and Oxygen/Sulfur-Impurity Effects on Oxidation and Nitridation in Single- and Two-Phase Cr–Nb Alloys, Oxid. Met. 58 (2002) 297–318. https://doi.org/10.1023/A:1020154620928.
[42] M.P. Brady, P.F. Tortorelli, E.A. Payzant, L.R. Walker, Oxidation Behavior of Cr 2 N, CrNbN, and CrTaN Phase Mixtures Formed on Nitrided Cr and Laves-Reinforced Cr Alloys, Oxid. Met. 61 (2004) 379–401. https://doi.org/10.1023/B:OXID.0000032330.95411.ec.
[43] A.S. Ulrich, U. Glatzel, M.C. Galetz, Discontinuities in Oxidation Kinetics: A New Model and its Application to Cr–Si-Base Alloys, Oxid. Met. 95 (2021) 445–465. https://doi.org/10.1007/s11085-021-10029-8.
[44] P. Pfizenmaier, A.S. Ulrich, M.C. Galetz, U. Glatzel, Tensile Creep Properties of Cr-Si Alloys at 980 °C in Air—Influence of Ge and Mo Addition, Metals 11 (2021) 1072. https://doi.org/10.3390/met11071072.
[45] A. Solimani, M. Schütze, A. Stark, M.C. Galetz, Nitrogen transport through thermally grown chromia scales, Corros. Sci. 145 (2018) 180–190. https://doi.org/10.1016/j.corsci.2018.10.007.
[46] A.S. Ulrich, Entwicklung von ausscheidungshärtbaren Cr-Si-Basis-Legierungen für Hochtemperaturanwendungen: Mikrostruktur und Oxidation, Shaker, Düren, 2020.
[47] G. Tammann, Über Anlauffarben von Metallen, Z. Anorg. Allg. Chem. 111 (1920) 78–89. https://doi.org/10.1002/zaac.19201110107.
[48] N.B. Pilling, R.E. Bedworth, Oxidation of Copper-Nickel Alloys at High Temperatures, Ind. Eng. Chem. 17 (1925) 372–376. https://doi.org/10.1021/ie50184a013.
[49] M.P. Brady, J.H. Zhu, C.T. Liu, P.F. Tortorelli, L.R. Walker, Oxidation resistance and mechanical properties of Laves phase reinforced Cr in-situ composites, Intermetallics 8 (2000) 1111–1118. https://doi.org/10.1016/S0966-9795(00)00046-7.